minerals

MDPI

Article

In Situ AFM Study of Crystal Growth on a Barite (001) Surface in $BaSO_4$ Solutions at 30 °C

Yoshihiro Kuwahara [1,*], Wen Liu [2], Masato Makio [2] and Keisuke Otsuka [2]

[1] Department of Environmental Changes, Faculty of Social and Cultural Studies, Kyushu University, Motooka, Fukuoka 819-0395, Japan

[2] Department of Comprehensive Earth Sciences, Graduate School of Integrated Sciences for Global Society, Kyushu University, Motooka, Fukuoka 819-0395, Japan; 2GS15057G@s.kyushu-u.ac.jp (W.L.); 3GS15017G@s.kyushu-u.ac.jp (M.M.); u77b22ced7pq96a@yahoo.co.jp (K.O.)

* Correspondence: ykuwa@scs.kyushu-u.ac.jp; Tel.: +81-92-802-5654

Academic Editor: Denis Gebauer

Received: 21 September 2016; Accepted: 24 October 2016; Published: 2 November 2016

Abstract: The growth behavior and kinetics of the barite (001) surface in supersaturated $BaSO_4$ solutions (supersaturation index (*SI*) = 1.1–4.1) at 30 °C were investigated using in situ atomic force microscopy (AFM). At the lowest supersaturation, the growth behavior was mainly the advancement of the initial step edges and filling in of the etch pits formed in the water before the $BaSO_4$ solution was injected. For solutions with higher supersaturation, the growth behavior was characterized by the advance of the <*uv*0> and [010] half-layer steps with two different advance rates and the formation of growth spirals with a rhombic to bow-shaped form and sector-shaped two-dimensional (2D) nuclei. The advance rates of the initial steps and the two steps of 2D nuclei were proportional to the *SI*. In contrast, the advance rates of the parallel steps with extremely short step spacing on growth spirals were proportional to SI^2, indicating that the lateral growth rates of growth spirals were directly proportional to the step separations. This dependence of the advance rate of every step on the growth spirals on the step separations predicts that the growth rates along the [001] direction of the growth spirals were proportional to SI^2 for lower supersaturations and to *SI* for higher supersaturations. The nucleation and growth rates of the 2D nuclei increased sharply for higher supersaturations using exponential functions. Using these kinetic equations, we predicted a critical supersaturation ($SI \approx 4.3$) at which the main growth mechanism of the (001) face would change from a spiral growth to a 2D nucleation growth mechanism: therefore, the morphology of bulk crystals would change.

Keywords: barite; atomic force microscopy (AFM); crystal growth; spiral growth; 2D nucleation growth

1. Introduction

Barite ($BaSO_4$) is the most abundant mineral of barium and occurs in a wide variety of geological environments that span geologic times from the Early Archean era to the present [1,2]. Barite is also one of the few marine authigenic minerals that are reported to form in the water column, as well as in marine sediments and locations around hydrothermal vents and cold seeps [3]. Due to its diverse modes of formation, barite can be utilized for paleoenvironmental, hydrogeological, and hydrothermal studies [3]. The precipitation and dissolution of barite control the concentration and mobility of Ba in the ground and surface water, due to its low solubility ($K_{sp} = 10^{-9.99}$ at 25 °C) in water [4,5]. The common scale mineral barite is also almost inevitable in industrial water, oil, and gas production systems due to its low solubility [4–9]. The uptake of radioactive Ra ions during barite formation [10] may occur from the systems from U mine wastes [2] or at a later stage of high-level waste-repository evolution [11] because Ra^{2+} and Ba^{2+} have a similar ionic radius and electronegativity.

Therefore, barite precipitation and dissolution reactions at the mineral–water interface are still substantial. Mineral growth in solutions preferentially occurs at kink sites, edges, steps, and defect outcrops, depending on the surface microtopography. Such microscopic growth features are also reflected in the bulk crystal appearance [12,13]. In situ Atomic Force Microscopy (AFM) allows direct observation of the growth and dissolution processes at the mineral–water interface at the site or step level (e.g., [9,14–16]). Several in situ AFM studies on barite growth, particularly on the (001) surface, which is a singular plane of barite, have been conducted to elucidate the processes involved and solve the problems cited above. The available AFM results mainly show two cases: one is growth on a singular interface with nucleus formation and spread (two-dimensional (2D) nucleation growth), and the other is growth on an imperfect singular interface, which controls the number of defect sites and the rate of lateral growth from these sites (spiral growth) (e.g., [4,8,13,17–23]). However, the available data and hypotheses regarding the growth kinetics of the two processes are still insufficient and unclear, although there are some reports regarding the lateral growth kinetics of steps or 2D islands {e.g., the lateral spreading rate of 2D islands is proportional to the supersaturation Ω (which is equivalent to IAP/K_{sp}, where IAP is the ion activity product of the ionic species in solution, $a(Ba^{2+})$ $a(SO_4{}^{2-})$, and K_{sp} is the solubility product of the growing mineral) [4,21]; the step velocity increases linearly with $S^{1/2}(S-1)$ where $S = \Omega^{1/2}$ [19]; and the 2D nucleation kinetics are shown by a linear correlation between ln N vs. $(\ln S)^{-1}$, where N is the density of the nuclei [21]}. In addition, the relationship between the anisotropic advance and retreat behaviors of the steps during barite growth and dissolution is not well understood.

In this study, we examined the growth behavior of the barite (001) surface in supersaturated $BaSO_4$ solutions at 30 °C using in situ AFM with an air/fluid heater/cooler system. The aims of this study were to reveal the microscopic growth behavior on the barite (001) surface at the step or site level and to estimate the growth kinetics of 2D nucleation and spiral growth that occur at the barite surface–aqueous solution interface, as well as the lateral advance rates of the initial steps, steps of the 2D nuclei, and steps on growth spirals.

2. Materials and Methods

2.1. Materials and Solutions

The barite ($(Ba_{0.98}Ca_{0.01}Sr_{0.01})SO_4$) used for this study was obtained from the Stonehem Barite Deposit in Colorado, USA in the form of a single optically clear crystal. The barite crystal was cleaved parallel to the (001) cleavage plane with a sharp knife blade immediately before the AFM observations and fixed on an AFM mount with an adhesive tab (Ted Pella, Inc., Redding, CA, USA). The crystallographic direction of the cleaved samples was determined from the morphology of the etch pit and/or the 2D nucleus [4,8,15]. Various steps were mechanically formed on the (001) surfaces by cleaving with the knife blade (e.g., Figures 1a and 2a), as shown in our previous studies on barite dissolution [15,16,24]. The initial steps were generally parallel to <uv0> (mainly <120>, <130>, <140>, and so on) and [010], but they did not necessarily appear to be oriented parallel to an energetically favorable crystallographic direction, and slightly curved steps were also observed. The step heights corresponded to a half-c unit cell layer (3.6 Å), a single unit cell layer (7.2 Å), and multiple layers.

The supersaturated $BaSO_4$ aqueous solutions were prepared by mixing Na_2SO_4 and $Ba(NO_3)_2$ solutions consisting of analytical grade chemicals and deionized water immediately before the AFM observations. The concentrations of the $BaSO_4$ solutions were 20–100 μM ($[Ba^{2+}]/[SO_4{}^{2-}] = 1$). The degree of supersaturation was calculated using the program PHREEQC (the database used was minteq) [25]. The supersaturation index (SI) can be expressed as

$$SI = \Delta\mu/kT = \ln(a/a_e) = \ln(\mathrm{IAP}/K_{sp}), \quad (1)$$

where Δμ is the difference in the chemical potential between the growth unit in the aqueous and solid phases, k is the Boltzmann constant, a is the activity of the ion species, and a_e is the equilibrium activity

at the temperature T [26–28]. The SI values of the $BaSO_4$ solutions were 1.1 for 20 μM, 2.4 for 40 μM, 3.2 for 60 μM, 3.7 for 80 μM, and 4.1 for 100 μM at 30 °C.

2.2. Barite Growth Experiments and AFM Imaging

In situ observations of barite growth were performed using a Nanoscope III with a Multimode SPM unit (Digital Instruments/Bruker AXS, Yokohama, Japan) and a fluid cell with an air/fluid heater/cooler system (Veeco/Bruker AXS, Yokohama, Japan), which was operated in contact-mode AFM (CMAFM) on a vibration isolation platform in a temperature- and humidity-controlled room [22]. The cleaved barite crystals were first reacted with pure water at 30 ± 0.3 °C to ensure stable AFM scanning conditions and obtain reliable AFM images. We then replaced the water with a $BaSO_4$ solution in the fluid cell and began observing the growth process on the barite (001) surface at 30 ± 0.3 °C. The temperature was controlled by the heater/cooler-stage and a Thermal Applications Controller (TAC) (Veeco/Bruker AXS); it was also monitored by a thermocouple thermometer (Cole-Parmer International, Vernon Hills, IL, USA) [22,29]. The pure water and $BaSO_4$ solutions flowed through the fluid cell at a constant rate of 0.6 mL/h, which was controlled by a syringe pump. The solution residence time in the fluid cell at the flow rate of 0.6 mL/h was approximately 8 min [22]. (Incidentally, we also attempted the growth experiments in the lowest and higher supersaturated (20, 80, and 100 μM) $BaSO_4$ solutions at a flow rate of 1.2 mL/h to examine the effect of the solution flow rate on the barite crystal growth. The growth rates of the 2D nuclei and growth spirals did not differ for the two flow rate conditions.)

The AFM images were captured at scan rates of 1 to 4 Hz with 512 × 512 scan lines (and also with 256 × 256 scan lines in the 100 μM $BaSO_4$ solutions only) using a specialized heater/cooler, J-head piezoelectric scanner (125 μm X-Y and 5 μm Z scan size) and oxide-sharpened Si_3N_4 tip units. The setpoint and direct scanning duration on the observed surface were kept as small as possible to reduce the scan force and minimize the effect of the tip on the sample surface. All experimental runs lasted over 2 h, and the longest experiment was over 9 h. We collected parallel CMAFM height and deflection images. The AFM images were analyzed using the methods described in our earlier studies [15,16] to determine the step advance rate and growth rates of islands and spirals. We did not use the AFM images obtained immediately after the water was replaced with the $BaSO_4$ solution in the fluid cell to estimate the nucleation rate of the 2D nuclei because the images did not show steady formation of the 2D nuclei.

3. Results

The growth behavior on the barite (001) surface changed as the supersaturation increased. At the lowest supersaturation (SI = 1.1), the growth behavior appeared to begin and persist with the advancement of the initial step edges and the filling in of the etch pits formed in water before the $BaSO_4$ solution was injected (Figure 1a,b). Although the formation of growth spirals from a screw dislocation was observed, their growth was extremely slow. Sector-shaped 2D nuclei, which were formed at higher supersaturations, were not observed at the lowest supersaturation.

The growth behavior of the moderate supersaturations (SI = 2.4–3.7) was characterized by the advance of two half-layer steps with distinctly different advance rates, the relatively rapid formation of growth spirals and hillocks, and the relatively slow formation of sector-shaped 2D nuclei (Figures 2 and 3). Of course, the advance rates of the various steps increased with increasing supersaturation (Table 1). Figure 2a–c reveals that the initial [010] one-layer steps were immediately split into two half-layer [010] steps with different advance rates. Similar results were also observed for the two half-layer [120] steps (Figure 3). The large difference in the advance rates of the "f" and the "s" steps led to the formation of a new one-layer step (Figure 3d).

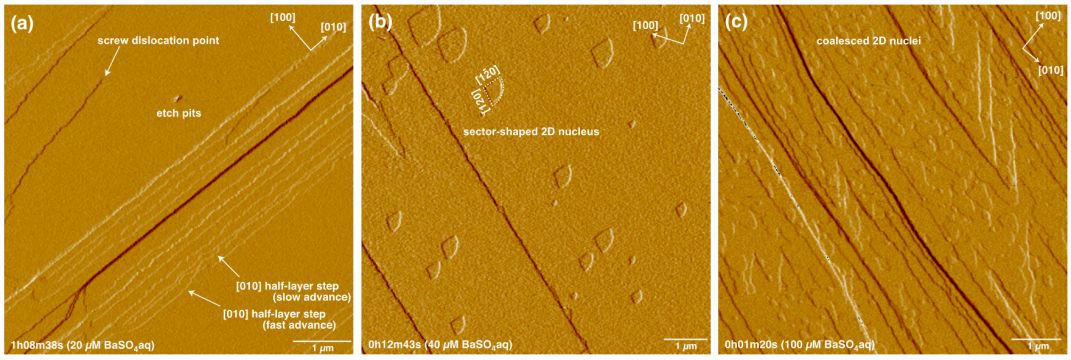

Figure 1. (**a**–**c**) CMAFM deflection images of a (001) surface in 20μM, 40 μM, and 100 μM $BaSO_4$ solutions at 30 °C, respectively. In (**b**), sector-shaped 2D nuclei formed sporadically, while in (**c**) these nuclei formed rapidly and coalesced.

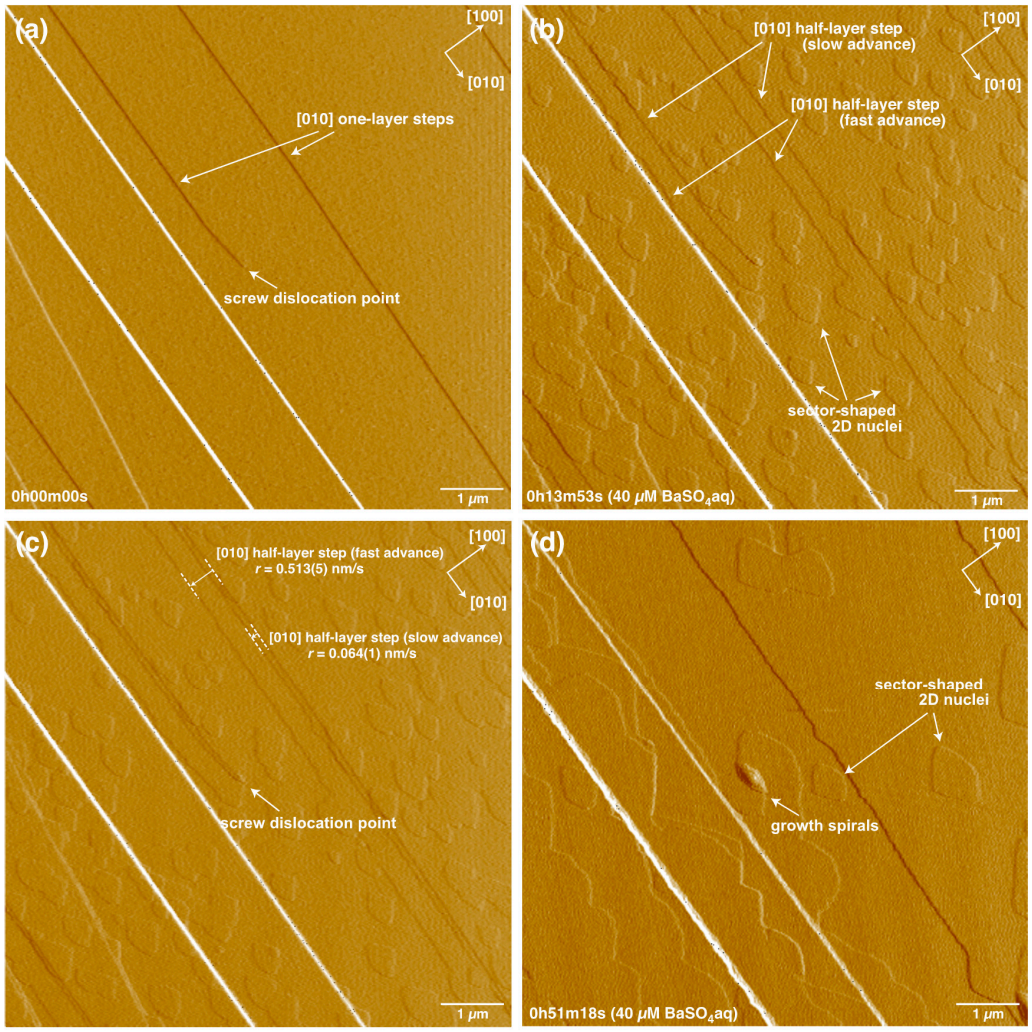

Figure 2. (**a**), (**b**), and (**d**) Sequential CMAFM deflection images of a (001) surface in a 40 μM $BaSO_4$ solution at 30 °C after 0 min, 14 min, and 51 min, respectively; each one-layer [010] step (step height = 7.2 Å) begins to split into two half-layer steps (step height = 3.6 Å) with different advance rates. Sector-shaped 2D nuclei were randomly formed, independent of the microtopography. In (**d**), the birth of a growth spirals that formed from a screw dislocation point is shown. (**c**) A comparison of (**a**) and (**b**), which are overlapped. The splitting process and advance rates of the steps are clearly demonstrated.

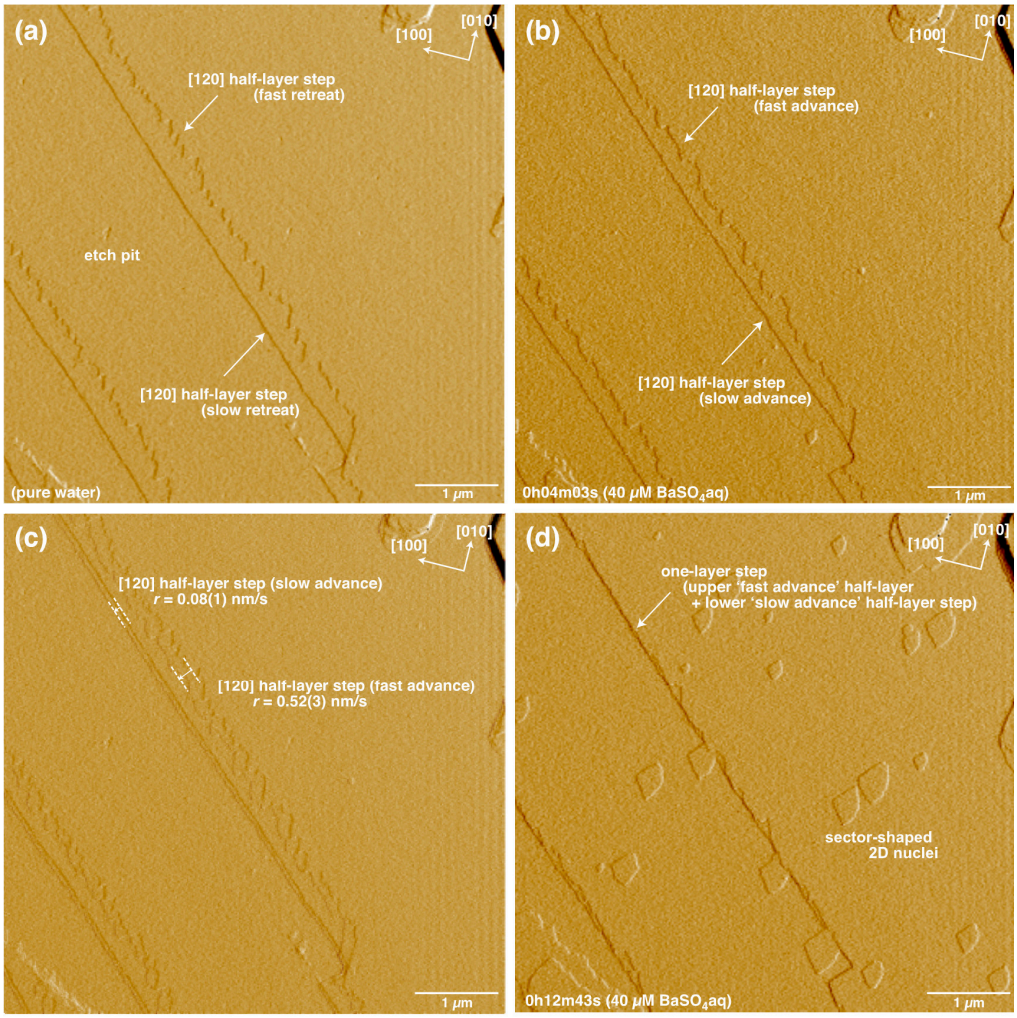

Figure 3. (**a**), (**b**), and (**d**) Sequential CMAFM deflection images of a (001) surface in pure water and in a 40 μM $BaSO_4$ solution at 30 °C after 4 min and 12 min, respectively. The [120] "fast retreat" and "slow retreat" half-layer steps during dissolution showed "fast advance" and "slow advance" behaviors, respectively, during growth. In (**d**), a new one-layer step was formed because the front of the half-layer step with the fast advance rate caught up with that of the immediately underlying half-layer step with the slow advance rate. (**c**) A comparison of (**a**) and (**b**), which are overlapped. The difference in the advance rate between the two [120] half-layer steps is clearly revealed.

Figure 2 also reveals the birth of growth spirals from a screw dislocation point at a moderate supersaturation (SI = 2.4). The morphology of the growth spirals was a rhombic form elongated along the [010] direction. The growth spirals tended to have a more curved outline with increasing supersaturation and showed mainly one-layer step sequences with approximately regular, narrow step spacings at each supersaturation condition (Figure 4). The growth rates of growth spirals also increased with increasing supersaturation (Table 2). Our AFM observations further captured the formation of growth hillocks where sector-shaped, half-layer 2D islands formed from a specific point were piled up and pointing in opposite orientations due to the presence of the 2_1 screw axis normal to the (001) plane, although these structures could only be observed at a moderate supersaturation (SI = 2.4) (Figure 4a). The growth hillocks may have formed from an edge dislocation point and grew slowly, while the growth spirals formed from a screw dislocation point grew rapidly.

The sector-shaped 2D nuclei were defined by half-layer steps parallel to [120], [1$\bar{2}$0], and a curved step edge tangent to [010] (Figures 2 and 3). Such sector-shaped 2D nuclei have been formed in

various supersaturated $BaSO_4$ solutions at room temperature {e.g., *SI* = 3 [8]; *SI* = 3.3 and 4.3 [18]; and *SI* = 4.0 and 4.5 [4]}. The [120] and curved steps of the 2D nuclei advanced at constant rates in each supersaturated solution for the duration of the experiment (i.e., the 2D nuclei grew at a constant rate) (Figures 5 and 6, Table 3).

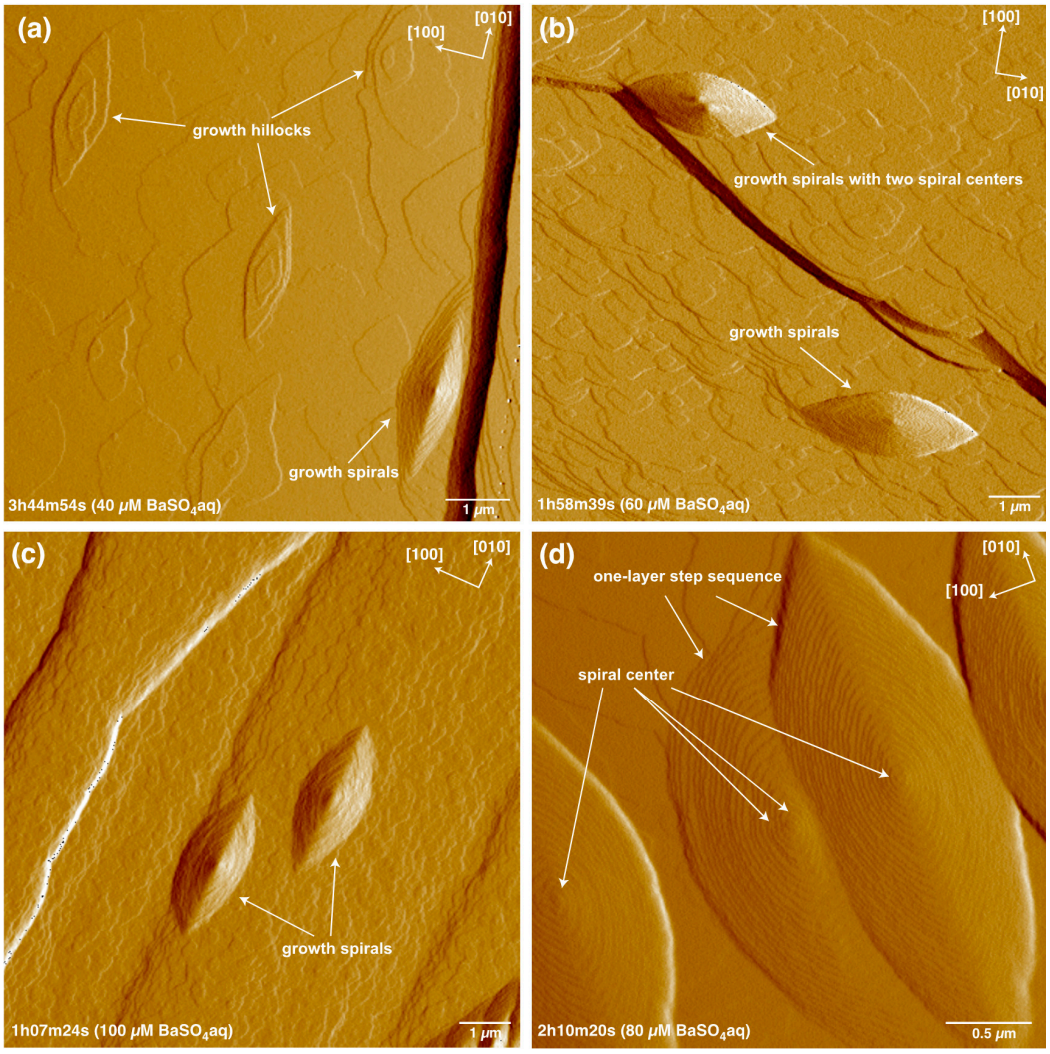

Figure 4. (**a**–**c**) CMAFM deflection images of a (001) surface in 40 μM, 60 μM, and 100 μM $BaSO_4$ solutions at 30 °C, respectively, showing the growth spirals that formed from screw dislocations. The growth hillocks that likely formed from edge dislocations are also shown in (**a**). (**d**) CMAFM deflection image of a (001) surface in an 80 μM $BaSO_4$ solution at 30 °C showing growth spirals with a one-layer step sequence and regular step spacing.

The growth behavior at the highest supersaturation (*SI* = 4.1) was characterized by the rapid formation and growth of sector-shaped 2D nuclei and growth spirals immediately after the solutions were injected into the AFM fluid cell (Figures 1d and 4c). We could not estimate the advance rates of initial steps and the [120] and curved steps of the 2D nuclei at higher supersaturations because the 2D nuclei formed and grew too rapidly, but we could estimate the nucleation rates of the 2D nuclei and the spiral growth rates. The bow-shaped growth spirals formed at the highest supersaturation showed a more curved outline than those for lower supersaturations, as mentioned above (Figure 4). A number of sector-shaped 2D nuclei immediately formed and coalesced on the initial surface, and new nuclei were deposited on the previous ones before a layer was completed (i.e., multi-nucleation growth [30]).

Table 1. Average advance rates of the various steps on the barite (001) surface.

$BaSO_4$ Concentration (μM)	Advance Rates of Steps on the (001) Surface (nm/s)				
	<*uv*0> * "f" Step with Half-Layer	<*uv*0> * "s" Step with Half-Layer	<*uv*0> * Step with One Layer ("f" upper + "s" Lower Half-Layers)	[010] "f" Step with Half-Layer	[010] "s" Step with Half-Layer
20	0.06 ± 0.01	0.03 ± 0.01	0.03 ± 0.01	0.05 ±0.01	0.02 ±0.01
40	0.50 ± 0.03	0.08 ± 0.01	0.12 ± 0.01	0.51 ± 0.02	0.07 ±0.01
60	0.62 ± 0.03	0.12 ± 0.01	0.21 ± 0.01	0.62 ± 0.03	0.11 ± 0.01
80	0.73 ± 0.05	0.16 ± 0.01	- **	- **	- **

* Mainly the <120> step, but also including the <130>, <140>, and other steps, as well as the slightly curved steps; ** These rates could not be estimated accurately, due to the rapid formation and growth of many 2D nuclei.

Table 2. Average spiral growth rates and step separations.

$BaSO_4$ Concentration (μM)	Face or Corner Advance Rates in the Growth Spirals			The Ratio of the Advance Rates in the Growth Spirals			Mean Step Separations * (nm)	
	[100] Corner (nm/s)	[010] Corner (nm/s)	(001) (nm/min)	(001)/[100]	(001)/[010]	[010]/[100]	[100]	[010]
20	(0.002) **	(0.006) **	(0.006) **					
40	0.04 ± 0.01	0.11 ± 0.01	0.11 ± 0.02	4.58×10^{-2}	1.67×10^{-2}	2.9	15.7	43.2
60	0.10 ± 0.01	0.25 ± 0.01	0.22 ± 0.05	3.67×10^{-2}	1.47×10^{-2}	2.5	19.6	49.1
80	0.13 ± 0.01	0.32 ± 0.02	0.26 ± 0.05	3.33×10^{-2}	1.35×10^{-2}	2.4	21.6	53.2
100	0.19 ± 0.02	0.46 ± 0.04	0.33 ± 0.09	2.89×10^{-2}	1.20×10^{-2}	2.4	24.9	60.2

* When every parallel step on the growth spirals is a one-layer step; ** These rates may be somewhat rough estimates, because they are calculated from only two data points and represent extremely slow spiral growth.

Table 3. Nucleation rates and average growth rates of the sector-shaped 2D nuclei.

$BaSO_4$ Concentration (μM)	Advance Rates of the Steps (nm/s)		Growth Rates toward the [001] Direction (nm/min)	Nucleation Rates (N/(μm^2·min))
	[120] Step	Curved Step		
40	0.08 ± 0.01	0.50 ± 0.02	0.012 ± 0.001	0.029 ± 0.007
60	0.12 ± 0.01	0.60 ± 0.02	0.022 ± 0.002	0.030 ± 0.008
80	0.16 ± 0.01	0.73 ± 0.05	0.041 ± 0.002	0.14 ± 0.08
100	- *	- *	0.21 ± 0.06	2.2 ± 0.3

* These rates could not be estimated accurately, due to the rapid formation and growth of many 2D nuclei.

Table 4. Growth rates of spiral growth and 2D growth on the barite (001) surface.

$BaSO_4$ Concentration (μM)	Spiral Growth Rate * ($\times 10^{-9}$ mol/(m^2·s))	2D Growth Rate ** ($\times 10^{-9}$ mol/(m^2·s))	Total Growth Rate ($\times 10^{-9}$ mol/(m^2·s))
40	1.3 ± 0.5	3.3 ± 0.8	5 ± 1
60	3.1 ± 1.2	3.7 ± 1.0	7 ± 2
80	4.0 ± 1.7	7.1 ± 4.1	11 ± 6
100	5.7 ± 2.4	20 ± 1	26 ± 4

* Using a = 0.8884 nm, b = 0.5456 nm, c = 0.7157 nm, density = 4.50 g/cm^3 [31], rate data in Table 2, and mean growth spirals density = 2 (±1) × 10^{12} m^{-2}; ** Using Equations (2) and (3), rate data in Table 3 as well as the above unit cell parameter and density [31].

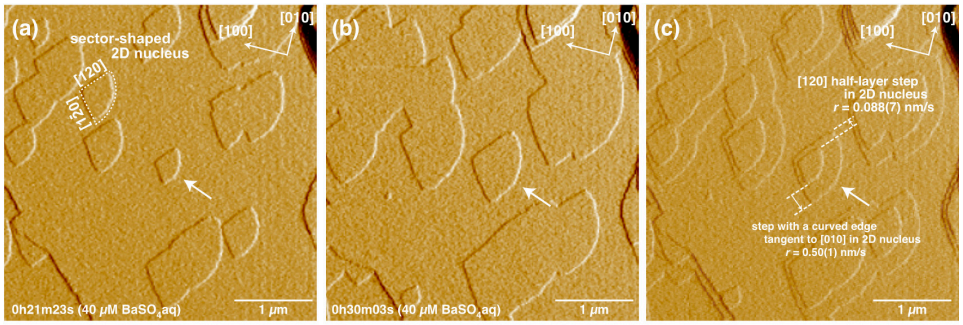

Figure 5. (**a**) and (**b**) Sequential CMAFM deflection images of a (001) surface in a 40 μM $BaSO_4$ solution at 30 °C after 21 min and 30 min, respectively; (**c**) a comparison of (**a**) and (**b**), which are overlapped. The lateral spreading process and step advance rates of the 2D nuclei are clearly demonstrated. See Figure 6 for the growth of a 2D nucleus that is indicated by the white arrows.

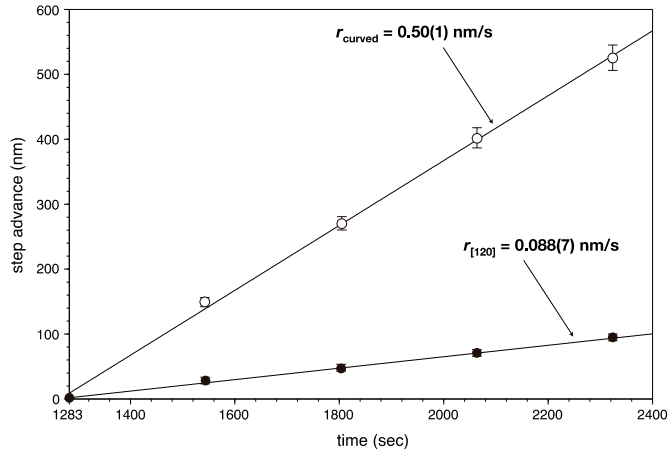

Figure 6. Changes in the [120] (solid circulars) and curved (open circulars) step advance distances in the 2D nucleus shown in Figure 5 as a function of time. We began measuring the step advance distance 21 min (Figure 5a) after the experiment began. The solid and open circular marks at 1803 s indicate the advance distances of the two steps in the 2D nucleus indicated by a white arrow in Figure 5b.

4. Discussion

4.1. Advance and Retreat Behavior of the Steps

Previous AFM studies on barite growth and dissolution reported that the <*uv*0> and [010] half-layer steps on the barite (001) surface have two different advance rates or retreat rates {e.g., step retreat (dissolution) [4,15,16,24,32]; step advance (growth) [17,18,21]}. However, the relationship between the anisotropic advance and retreat behaviors of the half-layer steps during barite growth and

dissolution is not entirely understood or delineated. Our AFM observations revealed that the [010] "fast retreat" and "slow retreat" half-layer steps during dissolution in water shifted to "slow advance" and "fast advance" steps, respectively, during growth in the supersaturated solution (Figures 1 and 2). In contrast, the [120] "fast retreat" and "slow retreat" half-layer steps during dissolution showed "fast advance" and "slow advance" behaviors, respectively, during growth (Figure 3). The results of this study and our previous AFM studies on barite dissolution [15,16,24] lead to a schematic model showing the relationships between the advance and retreat behaviors of the half-layer steps, the reduction and growth of the etch pits, and the growth of the sector-shaped 2D islands during barite growth and dissolution on the barite (001) surface (Figure 7). What is the cause of the differences in the advance behaviors of the two half-layer steps? A possible cause is that the [120] and [010] steps have the opposite termination (obtuse or acute), in which the acute steps advance more slowly than the obtuse steps [33]. Another important result is that the rate-limiting reaction for Ba attachment and detachment involves escape of the ion from the inner-sphere adsorbed species [34]. Stack et al. [34,35] demonstrated that the rate-limiting reaction of Ba attachment to a step is the change from inner-sphere adsorbed species involving only one bond to a surface sulfate to the bidentate species where the departing Ba makes two bonds to two surface sulfates. The state of inner-sphere adsorbed species may affect the step advancing rate.

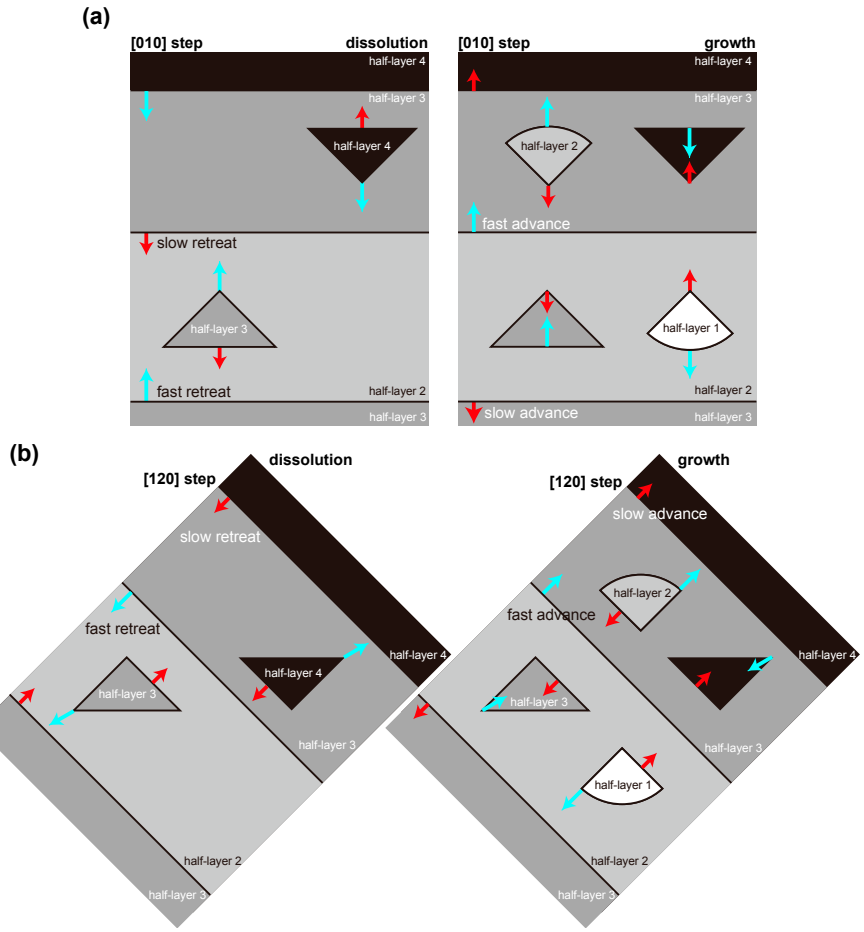

Figure 7. Schematic diagrams showing the relationships between the advance and retreat behaviors of the half-layer [010] (**a**) and [120] (**b**) steps, the reduction and growth of the etch pits, and the growth of sector-shaped 2D islands during growth and dissolution on the barite (001) surface. The uppermost and lowermost half-layers show half-layer 1 (white) and half-layer 4 (black), respectively. The red and blue arrows show the directions and relative rates (slow and fast, respectively) of the advance and retreat of the steps.

The advance rates of the <*uv*0> half-layer steps and the [120] and curved steps in the 2D islands were roughly proportional to the supersaturation index (*SI*) (Figure 8):

$$v_{<uv0>\text{f-step}}\ (\text{nm/s}) = 0.25\ SI - 0.18\ (r = 0.985) \quad (2)$$

$$v_{<uv0>\text{s-step}}\ (\text{nm/s}) = 0.047\ SI - 0.026\ (r = 0.989), \quad (3)$$

where $v_{<uv0>\text{f-step}}$ and $v_{<uv0>\text{s-step}}$ are the advance rates of the <*uv*0> "f" and "s" steps, respectively, and r is the correlation coefficient. The direct proportionality between the advance rates of the individual steps and the *SI* may be expressed by the lateral growth law using Brice's model, which states that an energy barrier (ΔG_I) is required to transfer an atom from the growth phase to the crystal, and moving the first growth-phase atom into the crystal is exactly equivalent to moving one step on the growth face [36,37]:

$$f_1\ (= v_{\text{step}}) = A \cdot \Delta\mu/kT = A \cdot SI, \quad (4)$$

where f_1 is the rate of sideways growth, v_{step} is the step advance rate, and $A = sv \exp(-\Delta G_I/RT)$. In this second equation, s is the interlayer spacing for the particular face, v is the vibration frequency of the particles, and R is the gas constant. Equation (4) is equivalent to the equation for the advance rate of a step described by Burton et al. [38]. Another expression, where the step advance rates are proportional to $S^{1/2}(S-1)$, has been presented by Zhang and Nancollas [39,40]. However, the step advance rates in this study were not proportional to $S^{1/2}(S-1)$.

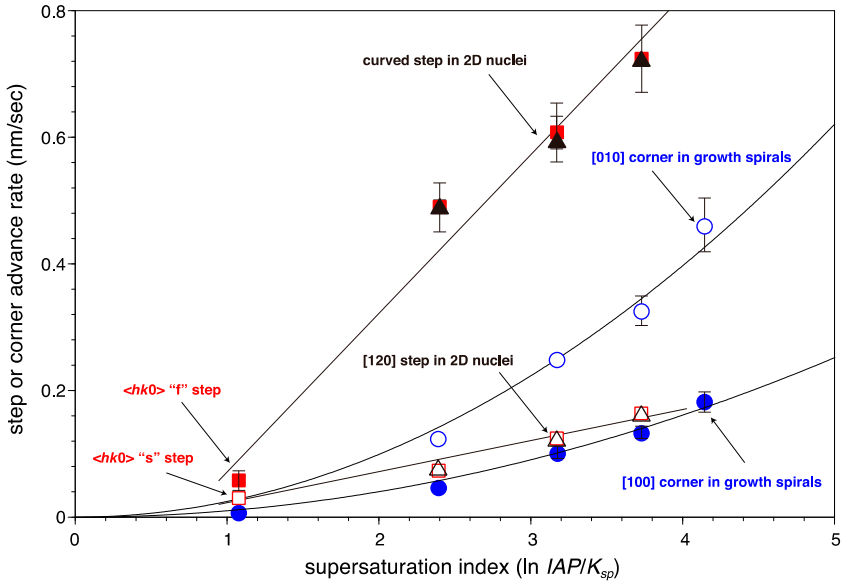

Figure 8. Changes in the step or corner advance rates of the initial steps, 2D nuclei, and growth spirals as a function of the supersaturation index (*SI*). The initial half-layer fast ("f") and slow ("s") steps were indicated by red solid and open squares, respectively. The [120] and curved steps in 2D nuclei were shown as open and solid triangles, respectively. The [010] and [100] corners of the growth spirals were indicated by blue open and solid circles, respectively. The lateral growth rates of the growth spirals were proportional to SI^2, while the advance rates of the initial steps and the two steps in the 2D nuclei were proportional to the *SI*.

4.2. Growth Spiral Formation and Development

The development of growth spirals formed from screw dislocations was somewhat complicated. The lateral growth rates of the growth spirals were proportional to SI^2 rather than *SI*, while the advance rates of the initial steps on the surface were proportional to *SI* (Figure 8):

$$f_{[010]}\ (\mathrm{nm/s}) = 0.025\ SI^2\ (r = 0.992) \quad (5)$$

$$f_{[100]}\ (\mathrm{nm/s}) = 0.010\ SI^2\ (r = 0.986), \quad (6)$$

where $f_{[010]}$ and $f_{[100]}$ are the advance rates of the [010] and [100] corners in the growth spirals, respectively. According to Burton et al. [38], a better derivation for Equation (4) yields

$$f_1 = v_{\mathrm{step}} = A\ SI\ \tanh(\lambda/2x_s), \quad (7)$$

where λ is the step separation in the parallel step sequence and x_s is the mean displacement of the adsorbed molecules ($2x_s$ is the catchment area of a step for adsorbed molecules [30]). Equation (7) reduces to Equation (4) when $\lambda >> 2x_s$ (namely, single steps or a step sequence where the step spacing is sufficiently wider than the catchment area of every step) and when $\lambda << 2x_s$, the equation predicts that

$$f_1 = v_{\mathrm{step}} = A\ \lambda\ SI/2x_s. \quad (8)$$

Equation (8) indicates that the advance rate of every step in a parallel step sequence is proportional to the spacing between the parallel steps when the step spacing is sufficiently shorter than the catchment area of every step, generally in higher supersaturations [30]. The slopes (p) of the [100] and [010] directions of the growth spirals ($R_{sp}/f_{[100]}$ and $R_{sp}/f_{[010]}$, respectively, where R_{sp} is the vertical growth rate of the growth spirals) in this study tended to gradually decrease with SI (Table 3). This result indicates that the mean step separations (λ) of parallel steps on the growth spirals were proportional to SI because the growth spirals showed mainly one-layer step sequences and approximately regular step spacings at each supersaturation (Table 3, Figure 4d). Thus, Equation (8) can be represented as:

$$f_1 = v_{\mathrm{step}} = A_2\ SI^2, \quad (9)$$

where A_2 is a constant. Indeed, the lateral growth rates of the growth spirals in our AFM experiments were directly proportional to the step separations (Figure 9) and proportional to SI^2 (Figure 8, Equations (5) and (6)).

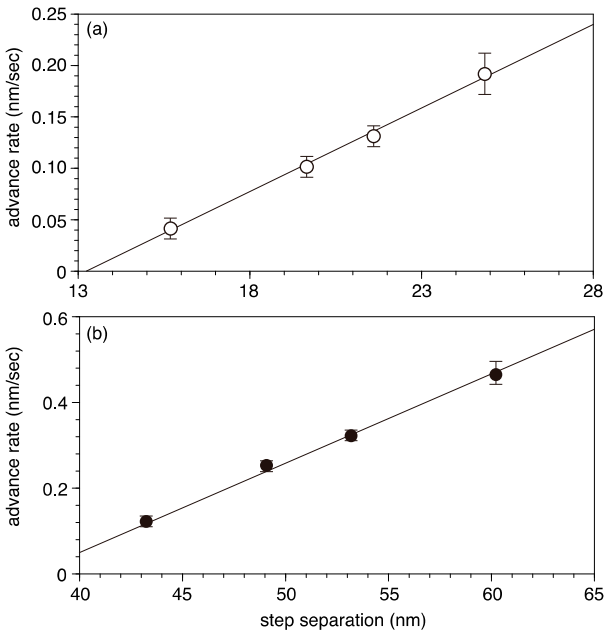

Figure 9. Changes in the lateral advance rates of parallel steps on the growth spirals as a function of the mean step separations of those that were proportional to SI. (**a**) Toward the [100] direction; (**b**) toward the [010] direction.

Pina et al. [17] explained the inhibition of the spiral growth through the structural control and anisotropy of the growth. On the (001) surface, alternate $BaSO_4$ layers are related by a 2_1 screw axis so that the anisotropy and the shape of the nuclei are reversed in each growth layer. The growth of the first $BaSO_4$ layer around the dislocation is restricted to one sector and cannot continue around the spiral because of the very slow growth in the opposite direction. In the next layer that forms around the dislocation, the directions are reversed but the rapid growth along is almost completely prevented by the very slow growth in the underlying layer. This alternation of fast and slow directions continues for subsequent layers and so growth around the screw dislocation is limited to an ever-tightening spiral. Similar results were also shown in anhydrite (100) and cerestite (001) growth [17,41].

The growth rate normal to the surface by spiral growth from a screw dislocation (R_{sp}) has been described by some well-known classical growth models (e.g., [37,38,42,43]):

$$R_{sp} = pv_{step} = dv_{step}/\lambda = dA\ SI \tanh(\lambda/2x_s)/\lambda, \quad (10)$$

where d is the height of a step. For $\lambda >> 2x_s$, Equation (10) predicts that

$$R_{sp} = dA\ SI/\lambda. \quad (11)$$

Here, the step separation (λ) of parallel steps on the growth spirals depends on the critical radius (ρ_c) of a central island [30,36]:

$$\lambda = 4\pi\rho_c \quad (12)$$

$$\rho_c = \kappa V/\Delta\mu = \gamma V/kTS, \quad (13)$$

where κ is the step edge free energy and V is the molar volume. From Equations (12) and (13),

$$1/\lambda \propto SI, \quad (14)$$

therefore

$$R_{sp} = A_3\ SI^2, \quad (15)$$

where A_3 is a constant. On the other hand, for $\lambda << 2x_s$, Equation (10) can be written in the form

$$R_{sp} = dA\ SI/2x_s = A_4\ SI, \quad (16)$$

where A_4 is a constant.

The growth rates (R_{sp}) of the growth spirals formed on the barite (001) surface appeared to be proportional to SI^2 (Figure 10), similar to the lateral growth rates ($f_{[010]}$ and $f_{[100]}$) (Figure 8). Thus,

$$R_{sp}\ (\text{nm/min}) = 0.019\ SI^2\ (r = 0.995). \quad (17)$$

However, the aforementioned dependence of the advance rate of every step on the growth spirals on the step separations or a proportional relationship between the lateral growth rates of the growth spirals and SI^2 predicts that the step separations would be significantly shorter than the catchment area of every step ($\lambda << 2x_s$). Hence, at least for SI = 2.4–4.1 at 30 °C, where the lateral growth rates of growth spirals clearly depended on the step separations (Figure 9), the growth rates (R_{sp}) of the growth spirals likely followed the growth law described in Equation (16) (Figure 10):

$$R_{sp}\ (\text{nm/min}) = 0.124\ SI - 0.187\ (r = 0.993). \quad (18)$$

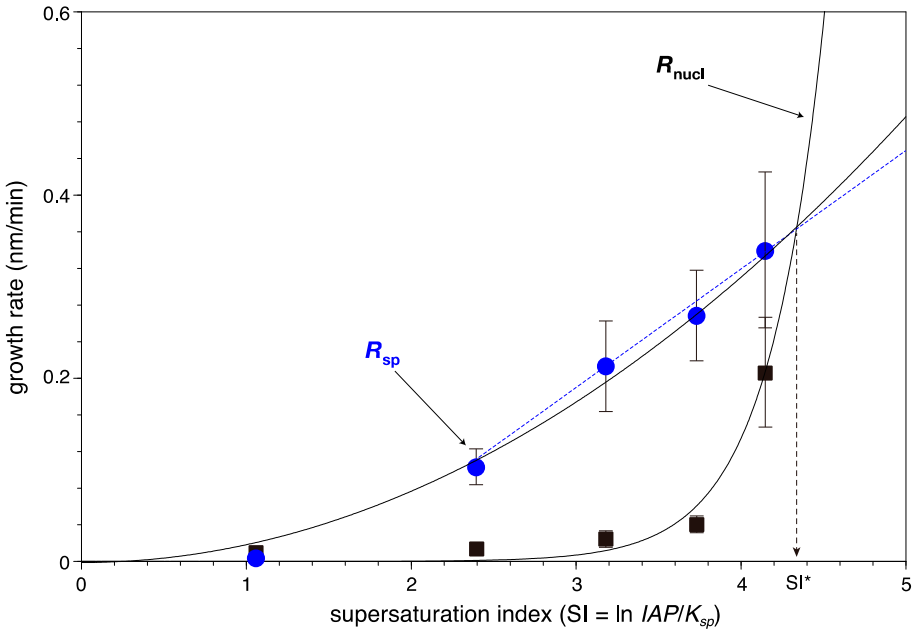

Figure 10. Changes in the growth rates toward the [001] direction of the growth spirals (R_{sp}) (blue solid circles) and 2D nuclei (R_{nucl}) (solid squares) as a function of the supersaturation index (SI). The growth rates (R_{sp}) of the growth spirals were likely proportional to SI^2 for lower supersaturations (a solid line) and to SI for higher supersaturations (a blue dotted line). In contrast, the growth rates (R_{nucl}) of the 2D nuclei increased sharply at higher supersaturations ($SI \geq 3.8$) and followed an exponential function (see text). It is expected that the main growth mechanism of the (001) face changes from a spiral growth to a 2D nucleation growth mechanism at an SI^* of approximately 4.3.

4.3. Formation and Growth of 2D Nuclei

The nucleation frequency and growth rate of the 2D nuclei on the singular interface have also been described by some growth models (e.g., [30,36,37,44]). According to their models, two limiting cases can be considered. The first case is the one where the nuclei rapidly grow laterally, namely, single nucleation growth, and the second case is one where the nuclei, once formed, spread slowly, such that new nuclei form on the old ones before layer growth is complete, namely, multi-nucleation growth. Here, our AFM observations revealed that the formation and growth of the 2D nuclei on the barite (001) surface followed the second limiting case (Figure 1). The nucleation frequency (J_L) of the 2D nuclei in the second limiting case [37] is:

$$J_L = A_5 \exp(-\Delta G^*/kT), \tag{19}$$

where A_5 is a constant and ΔG^* is the free energy of the nucleus:

$$\Delta G^* = \pi \rho_c \kappa. \tag{20}$$

Using Equations (13) and (20), Equation (19) can be written in the form

$$J_L = A_5 \exp(-B/SI), \tag{21}$$

where $B = \pi V \kappa^2$. Fitting our AFM data to Equation (21), we obtain a relationship between the formation frequency of 2D nuclei on the barite (001) surface and the SI (Figure 11):

$$J_L \ (\mathrm{N}/(\mu\mathrm{m}^2 \cdot \mathrm{min})) = 1.23 \times 10^{11} \exp(-1.03 \times 10^2/SI) \ (r = 0.999). \tag{22}$$

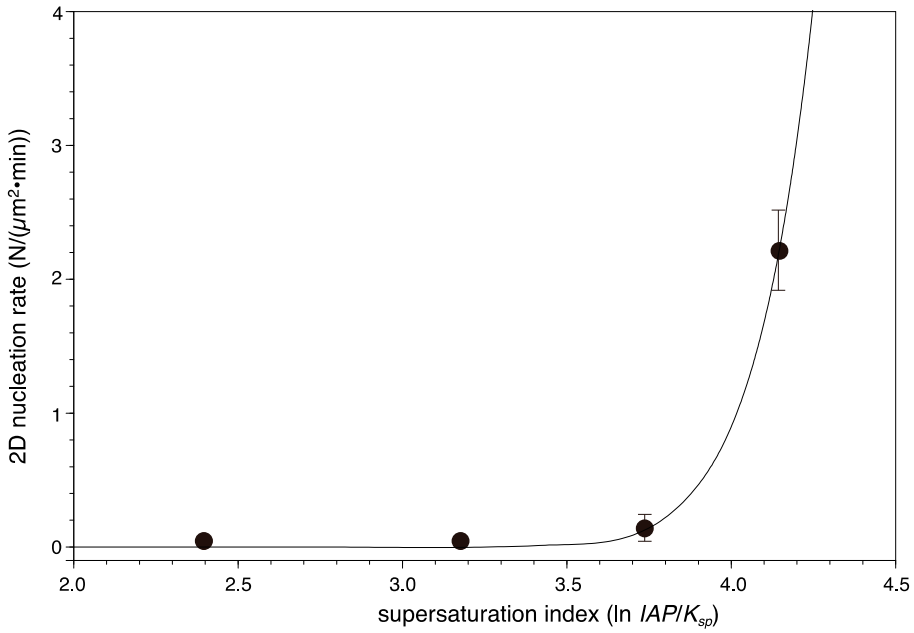

Figure 11. Changes in the 2D nucleation rates as a function of the supersaturation index (*SI*). The 2D nucleation rates increased sharply at higher supersaturations ($SI \geq 3.8$) and followed an exponential function, similar to the growth rates (R_{nucl}) of the 2D nuclei.

Similar results showing that there is a sharp increase in the nucleation rate above a certain high supersaturation level have been reported in previous AFM studies of the barite growth at different temperatures [4,21]. The supersaturation index (*SI*) above which there is a sharp increase in the nucleation rate was approximately 4.1 at 30 °C in this study and 4.2 at 22 °C in a previous study [4].

The vertical growth rate (R_{nucl}) of 2D nucleation growth in the first limiting case of Brice's model is represented as

$$R_{nucl} = d\, J_S, \tag{23}$$

where d is the step height of the nucleus and J_S is the formation frequency of the 2D nuclei in the first limiting case [36]. In the second limiting case, the growth rate is the cube root of the volume deposited in unit time:

$$R_{nucl} = (d\pi f_1^2 J_L)^{1/3}. \tag{24}$$

Using Equations (4) and (21), Equation (24) can be written in the form

$$R_{nucl} = A_6\, SI^{2/3} \exp(-B/SI), \tag{25}$$

where A_6 is a constant for a given material. Again, fitting our AFM data to Equation (25), we predict that the growth rates (R_{nucl}) of 2D nucleation growth on the barite (001) surface followed the growth law of Equation (25) (Figure 10):

$$R_{nucl} = 4.89 \times 10^4\, SI^{2/3} \exp\,(-5.51 \times 10^1/\mathrm{SI})\ (r = 0.993). \tag{26}$$

The lateral spreading rates of the sector-shaped 2D nuclei appeared to be proportional to the supersaturation index (*SI*), similar to the advance rates of the initial steps (Figure 8). The advance rates of the curved steps of the 2D nuclei were much higher than those of the [120] steps, although the difference in the rates gradually decreased with supersaturation (approximately 6.3 times at $SI = 2.4$ to 4.6 times at $SI = 3.7$) and was smaller than that (approximately 10 times) at a lower temperature (22 °C) in previous studies [4,21].

4.4. Implication of Microscopic Growth Kinetic Data for Macroscopic Features

Macroscopic barite growth rates reported in the previous studies showed 10^7–10^8 mol/(m^2·s) at a range of $3 < SI < 5$ at room temperature (e.g., [21,45]). The macroscopic growth rates are approximately an order of magnitude higher than the growth rates on the (001) surface that were estimated from our AFM data (Table 4). A possible cause of the difference is the growth of other surfaces that are faster than the growth of the (001) surface. Godinho and Stack [45] showed that growth rates of the {010} and {210} surfaces were significantly and slightly higher than that of the {001} surface, respectively. Another possible cause is the difference in the dislocation density (or growth spirals density). Boshbach [21] showed that the observed dislocation density on the (001) surface was up to 10^{13} m^{-2} and led to a macroscopic growth rate of about 10^{-8} mol/(m^2·s). Using the dislocation density instead of our growth spirals density data (2×10^{12} m^{-2}), we can also estimate growth rates of the (001) surface of about 10^{-8} mol/(m^2·s).

It is important to understand the process by which minerals that are naturally grown in solutions form to transfer microscopic growth features to macroscopic features [12]. Several studies on barite crystals in hydrothermal fluid or cold seep have reported that they increase in size and change their morphologies from platy to rectangular, prismatic or dendritic with the degree of supersaturation [3,46–48]. Kowacz and Putnis [13] have demonstrated that the nanoscale morphology of the growth features on the barite (001) surface in a supersaturated solution with 0.03 M KCl was reflected in the morphology of the bulk crystals (~10 μm in size) precipitated from the solution of the corresponding composition. The pseudo-hexagonal shape of the (001) face and elongation of the bulk crystals correlate with the hexagonal shape of the growth spirals and the very narrow layer spacing on the growth spirals that corresponds to its preferential growth in the direction normal to the (001) surface with little lateral spreading. Using four empirical kinetic equations (Equations (2), (5), (17) or (18) and (26)), we can estimate that for $SI < 4$, where the growth of the (001) face was mainly controlled by a spiral growth mechanism, the ratio (R_{sp}/f_1) of the vertical growth rates to the lateral advance rates of the growth spirals was one to two orders of magnitude higher than that (R_{nucl}/v_{step}) of the 2D nuclei. This result was consistent with the results reported by Kowacz and Putnis [13].

The 2D nuclei on the barite (001) surface were randomly distributed independent of the microtopography, similar to the nucleation under different conditions in previous AFM studies on barite growth [4,13,18]. Using two growth kinetic equations (Equations (18) and (26)), we can predict a critical supersaturation ($SI^* \approx 4.3$) at which the main growth mechanism of the (001) face would change from a spiral growth mechanism to a 2D nucleation growth mechanism (Figure 10). Therefore, over the critical supersaturation SI^*(≈4.3) the development of larger crystals with a wider singular (001) surface {e.g., tabular crystals bounded by {210} (closely related to the [120] and [1$\bar{2}$0] steps, with much slower advance rates than the curved step of 2D nuclei) precipitated from sea water or (low temperature) hydrothermal solutions [3,47]} may be predicted, due to the rapid nucleation and faster lateral spreading of the 2D nuclei. Interestingly, Pina et al. [49] reported that the transitional supersaturation values where 2D nuclei were observed for the first time were approximately $SI = 1.9$ for barite and $SI = 0.8$ for selestite, predicting the decrease of the critical supersaturation SI^* with increasing celestite composition in the (Ba,Sr)SO_4 solid solution.

The formation and growth of barite from aqueous supersaturated solutions are a well-known problem in industrial oil and gas production systems. Recent experimental studies on the coating of barite from supersaturated solutions in the absence of chemical scale inhibitors on a stainless steel surface have revealed the oriented crystallization where the (001) face mainly developed [50,51]. Our kinetic data regarding the vertical growth of the barite (001) face are certainly helpful in estimating the thickness of the barite film formed under such conditions. For instance, Equations (18) and (26), which predict the sharp increase of the growth rate of the barite (001) face over a critical supersaturation, estimate that the vertical growth rate of the (001) face rises more than two-fold when the SI increases from 4.0 to 4.5, while it increases only by 1.2-fold when the SI increases from 3.5 to 4.0. This explains

why barite crystals deposited on a quartz crystal microbalance (QCM) surface at the highest *SI* (4.32) were considerably larger than those at the lower *SI* [52].

5. Conclusions

Our in situ AFM study carefully examined the microscopic growth behavior on the barite (001) surface at 30 °C and revealed the mechanisms and kinetics of barite growth across a range of supersaturation conditions. Regarding lateral growth on the barite (001) surface, the advance rates of the parallel steps with extremely short step spacings on the growth spirals were proportional to the square of the supersaturation index (SI^2), while those of the initial steps and the two steps of the 2D nuclei (namely, single steps or steps with wider step spacings) were proportional to *SI*. On the other hand, the growth perpendicular to the (001) surface was mainly controlled by a spiral growth mechanism, where the growth rates (R_{sp}) of the growth spirals were proportional to SI^2 for lower supersaturations and to *SI* for higher supersaturations. However, over a critical supersaturation ($SI \approx 3.8$) the nucleation rates (J_L) and growth rates (R_{nucl}) of the 2D nuclei formed on the (001) surface increased sharply and followed exponential functions. These microscopic and kinetic data on barite growth help us to predict and improve the growth processes and rate laws.

Acknowledgments: The authors thank K. Ishida, Y. Nakamuta, and S. Uehara of Kyushu University for their helpful suggestions. We also thank the three anonymous reviewers for their thorough reviews that improved the quality of the study. This study was supported in part by a Grant-in-Aid for Scientific Research (Y. Kuwahara, No. 26400518) from the Japan Society for the Promotion of Science.

Author Contributions: Yoshihiro Kuwahara and Wen Liu conceived and designed the experiments; Yoshihiro Kuwahara, Wen Liu, and Keisuke Otsuka performed the experiments; all authors analyzed the data; Yoshihiro Kuwahara, Wen Liu, and Masato Makio contributed reagents/materials/analysis tools; Yoshihiro Kuwahara wrote the paper.

Conflicts of Interest: The authors declare no conflict of interest.

References

1. Gaines, R.V.; Skinner, H.C.W.; Foord, E.E.; Mason, B.; Rosenzweig, A. *Dana's New Mineralogy*, 8th ed.; John Wiley & Sons: New York, NY, USA, 1997; pp. 571–582.
2. Hanor, J.S. Barite-Celestine geochemistry and environments of formation. In *Sulfate Minerals–Crystallography, Geochemistry, and Environmental Significance. Reviews in Mineralogy and Geochemistry*; Alpers, C.N., Jambor, J.L., Nordstrom, D.K., Eds.; Mineralogical Society of America: Chantilly, VA, USA, 2000; Volume 40, pp. 193–275.
3. Griffith, E.M.; Paytan, A. Barite in the ocean—Occurrence, geochemistry and palaeoceanographic applications. *Sedimentology* **2012**, *59*, 1817–1835. [CrossRef]
4. Bosbach, D.; Hall, C.; Putnis, A. Mineral precipitation and dissolution in aqueous solution: In-situ microscopic observations on barite (001) with atomic force microscopy. *Chem. Geol.* **1998**, *151*, 143–160. [CrossRef]
5. Putnis, C.V.; Kowacz, M.; Putnis, A. The mechanism and kinetics of DTPA-promoted dissolution of barite. *Appl. Geochem.* **2008**, *23*, 2778–2788. [CrossRef]
6. Wang, K.S.; Resch, R.; Koel, B.E.; Shuler, P.J.; Tang, Y.; Chen, H.J. Study of the dissolution of the barium sulfate (001) surface with hydrochloric acid by atomic force microscopy. *J. Colloid Interface Sci.* **1999**, *219*, 212–215. [CrossRef] [PubMed]
7. Wang, K.S.; Resch, R.; Dunn, K.; Shuler, P.; Tang, Y.; Koel, B.E.; Yen, T.F. Dissolution of the barite (001) surface by the chelating agent DTPA as studied with non-contact atomic force microscopy. *Colloids Surf.* **1999**, *160*, 217–227. [CrossRef]
8. Risthaus, P.; Bosbach, D.; Becker, U.; Putnis, A. Barite scale formation and dissolution at high ionic strength studied with atomic force microscopy. *Colloids Surf.* **2001**, *191*, 201–214. [CrossRef]
9. Becker, U.; Biswas, S.; Kendall, T.; Risthaus, P.; Putnis, C.V.; Pina, C.M. Interactions between mineral surfaces and dissolved species: From monovalent ions to complex organic molecules. *Am. J. Sci.* **2005**, *305*, 791–825. [CrossRef]

10. Brandt, F.; Curti, E.; Klinkenberg, M.; Rozov, K.; Bosbach, D. Replacement of barite by a (Ba,Ra)SO_4 solid solution at close-to-equilibrium conditions: A combined experimental and theoretical study. *Geochim. Cosmochim. Acta* **2015**, *155*, 1–15. [CrossRef]
11. Culti, E.; Fujiwara, K.; Iijima, K.; Tits, J.; Cuesta, C.; Kitamura, A.; Glaus, M.A.; Müller, W. Radium uptake during barite recrystallization at 23 ± 2 °C as a function of solution composition: An experimental ^{133}Ba and ^{226}Ra tracer study. *Geochim. Cosmochim. Acta* **2010**, *74*, 3553–3570.
12. De Yoreo, J.J.; Dove, P.M. Shaping crystals with biomolecules. *Science* **2004**, *306*, 1301–1302. [CrossRef] [PubMed]
13. Kowacz, M.; Putnis, A. The effect of specific background electrolytes on water structure and solute hydration: Consequences for crystal dissolution and growth. *Geochim. Cosmochim. Acta* **2008**, *72*, 4476–4487. [CrossRef]
14. Bosbach, D.; Charlet, L.; Bickmore, B.; Hochella, M.F., Jr. The dissolution of hectorite: In-situ, real-time observations using atomic force microscopy. *Am. Mineral.* **2000**, *85*, 1209–1216. [CrossRef]
15. Kuwahara, Y. In situ Atomic Force Microscopy study of dissolution of the barite (001) surface in water at 30 °C. *Geochim. Cosmochim. Acta* **2011**, *75*, 41–51. [CrossRef]
16. Kuwahara, Y. In situ hot-stage AFM study of the dissolution of the barite (001) surface in water at 30–55 °C. *Am. Mineral.* **2012**, *97*, 1564–1573. [CrossRef]
17. Pina, C.M.; Becker, U.; Risthaus, P.; Bosbach, D.; Putnis, A. Molecular-scale mechanisms of crystal growth in barite. *Nature* **1998**, *395*, 483–486.
18. Pina, C.M.; Bosbach, D.; Prieto, M.; Putnis, A. Microtopography of the barite (001) face during growth: AFM observations and PBC theory. *J. Cryst. Growth* **1998**, *187*, 119–125. [CrossRef]
19. Higgins, S.R.; Bosbach, D.; Eggleston, C.M.; Knauss, K.G. Kink dynamics and step growth on barium sulfate (001): A hydrothermal scanning probe microscopy study. *J. Phys. Chem. B* **2000**, *104*, 6978–6982. [CrossRef]
20. Becker, U.; Risthaus, P.; Bosbach, D.; Putnis, A. Selective attachment of monovalent background electrolyte ions and growth inhibitors to polar steps on sulfates as studied by molecular simulations and AFM observations. *Mol. Simul.* **2002**, *28*, 607–632. [CrossRef]
21. Bosbach, D. Linking molecular-scale barite precipitation mechanisms with macroscopic crystal growth rates. In *Water-Rock Interactions, Ore Deposits, and Environmental Geochemistry: A Tribute to David A. Crerar*; Hellmann, R., Wood, S.A., Eds.; The Geochemical Society: St. Louis, MO, USA, 2002; Special Publication No. 7; pp. 97–110.
22. Kuwahara, Y.; Ishida, K.; Uehara, S.; Kita, I.; Nakamuta, Y.; Hayashi, T.; Fujii, R. Cool-stage AFM, a new AFM method for in situ observations of mineral growth and dissolution at reduced temperature: Investigation of the responsiveness and accuracy of the cooling system and a prelim experiment on barite growth. *Clay Sci.* **2012**, *16*, 111–119.
23. Ruiz-Agudo, C.; Putnis, C.V.; Putnis, A. The effect of a copolymer inhibitor on baryte precipitation. *Mineral. Mag.* **2014**, *78*, 1423–1430. [CrossRef]
24. Kuwahara, Y.; Makio, M. In situ AFM study on barite (001) surface dissolution in NaCl solutions at 30 °C. *Appl. Geochem.* **2014**, *51*, 246–254. [CrossRef]
25. Parkhurst, D.L.; Appelo, C.A.J. *User's Guide to PHREEQC (Version 2)—A Computer Program for Speciation, Batch-Reaction, One-Dimensional Transport, and Inverse Geochemical Calculations*; U.S. Geological Survey; U.S. Department of the Interior: Washington, DC, USA, 1999.
26. Henry Teng, H.; Dove, P.M.; De Yoreo, J.J. Kinetics of calcite growth: Surface processes and relationships to macroscopic rate laws. *Geochim. Cosmochim. Acta* **2000**, *64*, 2255–2266. [CrossRef]
27. Kowacz, M.; Putnis, C.V.; Putnis, A. The effect of cation: Anion ratio in solution on the mechanism of barite growth at constant supersaturation: Role of the desolvation process on the growth kinetics. *Geochim. Cosmochim. Acta* **2007**, *71*, 5168–5179. [CrossRef]
28. Zhang, F.; Yan, C.; Henry Teng, H.; Roden, E.E.; Xu, H. In situ AFM observations of Ca-Mg carbonate crystallization catalyzed by dissolved sulfide: Implications for sedimentary dolomite formation. *Geochim. Cosmochim. Acta* **2013**, *105*, 44–55. [CrossRef]
29. Kuwahara, Y. In situ observations of muscovite dissolution under alkaline conditions at 25–50 °C by AFM with an air/fluid heater system. *Am. Mineral.* **2008**, *93*, 1209–1216. [CrossRef]
30. Kuroda, T. *Crystal Lives (Kesshou-ha-ikiteiru): The Mechanism of Its Growth and Transformation of Morphology*; Science-sha: Tokyo, Japan, 1984. (In Japanese)
31. Hill, R.J. A further refinement of the barite structure. *Can. Mineral.* **1977**, *15*, 522–526.

32. Higgins, S.R.; Jordan, G.; Eggleston, C.M. Dissolution kinetics of the barium sulfate (001) surface by hydrothermal atomic force microscopy. *Langmuir* **1998**, *14*, 4967–4971. [CrossRef]
33. Bracco, J.N.; Gooijer, Y.; Higgins, S.R. Hydrothermal atomic force microscopy observantions of barite step growth rates as a function of the aqueous barium-to-sulfate ratio. *Geochim. Cosmochim. Acta* **2016**, *183*, 1–13. [CrossRef]
34. Stack, A.G.; Raiteri, P.; Gale, J.D. Accurate rates of the complex mechanisms for growth and dissolution of minerals using a combination of rare-event theories. *J. Am. Chem. Soc.* **2012**, *134*, 11–14. [CrossRef] [PubMed]
35. Stack, A.G. Molecular dynamics simulations of solvation and kink site formation at the {001} barite-water interface. *J. Phys. Chem. C* **2009**, *113*, 2104–2110. [CrossRef]
36. Brice, J.C. The Growth of Crystals from Liquids. In *Selected Topics in Solid State Physics*; Wohlfarth, E.P., Ed.; North-Holland Publishing Company: Amsterdam, The Netherlands, 1973.
37. Brice, J.C. *Crystal Growth Processes*; Blackie Halsted Press: Glasgow/London, UK, 1986.
38. Burton, W.K.; Cabrera, N.; Frank, F.C. The growth of crystals and the equilibrium structure of their surfaces. *Philos. Trans. R. Soc. Lond. A* **1951**, *243*, 299–358. [CrossRef]
39. Zhang, J.; Nancollas, G.H. Kink densities along a crystal surface step at low temperatures and under nonequilibrium conditions. *J. Cryst. Growth* **1990**, *106*, 181–190. [CrossRef]
40. Zhang, J.; Nancollas, G.H. Kink density and rate of step movement during growth and dissolution of an AB crystal in a nonstoichiometric solution. *J. Colloid Interface Sci.* **1998**, *200*, 131–145. [CrossRef]
41. Morales, J.; Astilleros, J.M.; Fernández-Díaz, L. Nanoscopic characteristics of anhydrite (001) growth. *Cryst. Growth Des.* **2012**, *12*, 414–421. [CrossRef]
42. Chernov, A.A. The Spiral Growth of Crystals. *Sov. Phys. Uspekhi* **1961**, *4*, 116–148. [CrossRef]
43. Chernov, A.A. *Modern Crystallography III. Crystal Growth*; Springer Series in Solid-State Science; Springer: Berlin/Heidelberg, Germany, 1984.
44. Walton, A.G. Nucleation in Liquids and Solutions. In *Nucleation*; Zettlemoyer, A.C., Ed.; Marcel Dekker Inc.: New York, NY, USA, 1969; pp. 225–307.
45. Godinho, J.R.A.; Stack, A.G. Growth kinetics and morphology of barite crystals derived from face-specific growth rates. *Cryst. Growth Des.* **2015**, *15*, 2064–2071. [CrossRef]
46. Shikazono, N. Precipitation mechanisms of barite in sulfate-sulfide deposits in back-arc basins. *Geochim. Cosmochim. Acta* **1994**, *58*, 2203–2213. [CrossRef]
47. Paytan, A.; Mearon, S.; Cobb, K.; Kastner, M. Origin of marine barite deposits: Sr and S isotope characterization. *Geology* **2002**, *30*, 747–750. [CrossRef]
48. Ray, D.; Kota, D.; Das, P.; Surya Prakash, L.; Khedekar, V.D.; Paropkari, A.L.; Mudholkar, A.V. Microtexture and distribution of minerals in hydrothermal barite-silica chimney from the Franklin seamount, SW Pacific: Constraints on the mode of formation. *Acta Geol. Sin.* **2014**, *88*, 213–225.
49. Pina, C.M.; Enders, M.; Putnis, A. The composition of solid solutions crystallising from aqueous solutions: The influence of supersaturation and growth mechanisms. *Chem. Geol.* **2000**, *168*, 198–210. [CrossRef]
50. Dinamani, M.; Kamath, P.V.; Seshadri, R. Electrochemical deposition of $BaSO_4$ coatings on stainless steel substrates. *Chem. Mater.* **2001**, *13*, 3981–3985. [CrossRef]
51. Mavredaki, E.; Neville, A.; Sorbie, K.S. Assessment of barium sulphate formation and inhibition at surfaces with synchrotron X-ray diffraction (SXRD). *Appl. Surf. Sci.* **2011**, *257*, 4264–4271. [CrossRef]
52. Mavredaki, E.; Neville, A.; Sorbie, K.S. Initial stages of barium sulfate formation at surfaces in the presence of inhibitors. *Cryst. Growth Des.* **2011**, *11*, 4751–4758. [CrossRef]